Int J Adv Manuf Technol (2016) 84:2537–2546
DOI 10.1007/s00170-015-7833-4

ORIGINAL ARTICLE

The systematic parameter optimization in the Nd:YAG laser beam welding of Inconel 625

M. R. Jelokhani-Niaraki[1] · N. B. Mostafa Arab[1] · H. Naffakh-Moosavy[2] · M. Ghoreishi[3]

Received: 27 May 2015 / Accepted: 10 September 2015 / Published online: 3 October 2015

Abstract This paper presents process parameter optimization for the laser welding of 0.5-mm-thick Inconel 625. The effect of laser parameters such as laser power (LP), spot size (SS), and welding speed (WS) on weld strength (WST) and microhardness of the welds has been investigated using the response surface methodology (RSM). A three-level design with 20 experimental runs was used. The analysis of variance (ANOVA) was performed and mathematical models were developed to predict the effect of input parameters on the responses. Results indicated that the maximum weld strength of 1280 MPa can be obtained when LP, WS, and SS are set at the optimum values of 260 W, 1.2 mm/s, and 180 μm, respectively. LP of 230 W, WS of 6 mm/s, and SS of 540 μm also resulted in minimum microhardness deviation (MHD) from that of the base metal. Higher heat input caused deeper penetration of weld joint and so higher WST. Formation of Laves phase in samples that receives higher energy density resulted in increase of microhardness and so MHD.

Keywords Laser welding · Inconel 625 · Response surface methodology · Weld strength · Microhardness

✉ N. B. Mostafa Arab
n.arab@srttu.edu

[1] Faculty of Mechanical Engineering, Shahid Rajaee Teacher Training University, Tehran, Iran

[2] Department of Materials Engineering, Faculty of Engineering, Tarbiat Modares University (TMU), Tehran, Iran

[3] Faculty of Mechanical Engineering, K. N. Toosi University of Technology, Tehran, Iran

1 Introduction

Nickel-based superalloys are one of the most important high-temperature materials that exhibit high tensile strength and high corrosion resistance even at high temperatures [1, 2]. In this context, the Inconel 625 alloy stands out as one of the leading commercial Ni–Cr–Mo–Nb alloy grades [3]. Service temperature range for this alloy is from cryogenic to 982 °C. Aerospace, power plant, and sea-water applications are fields that use Inconel 625 frequently [4–6].

One of the most effective welding techniques for joining high-temperature materials such as Inconel 625 is laser beam welding (LBW). Very low heat input, narrow heat-affected zone, high-energy density, high speed, good focusing characteristics, noncontact process, absence of vibration of the parts in the process, and the possibility of optimizing the welding heat are the advantages of LBW [7, 8]. Weld bead geometry, mechanical properties, and distortion are weld quality characteristics. During the welding process, the material properties like hardness, tensile strength, toughness, etc. can be changed. Thus, to obtain a welded joint with desired geometry, excellent mechanical properties, and minimum distortion, welding process parameters must be properly selected and adjusted. The weld quality is a function of the welding process parameters. The most important process parameters in LBW are the output power, welding speed, focal position, shielding gas, and position accuracy [9]. Various optimization methods are used to define the relationship between the input parameters and output variables. One of the most powerful and effective techniques is the design of experiments (DOE) technique that is used in a variety of industries to improve products or manufacturing processes [10]. Alrbaey et al. [11] performed a three-level full-factorial DOE to optimize the surface roughness of selective laser-melted stainless steel parts. It was found that the best obtainable final surface roughness was achieved

Table 1 Process input parameters and their levels

		Character −1	Parameter 0	Level 1
LP	Laser power (W)	230	245	260
WS	Welding speed (mm/s)	1.2	3.6	6
SS	Spot size (μm)	180	360	540

in a laser power of about 180 W. Kim et al.[12] applied a full-factorial design to determine the optimum laser-TIG (tungsten inert gas) hybrid welding process parameters for the lap joint of zinc-coated steel without a gap. They evaluated the weld quality by using the weight of the spatter. It was indicated that the weld quality was proportional to the laser beam-arc distance and the welding current and inversely proportional to the welding speed. M.M.A. Khan et al. [13] experimentally investigated the effect of LBW parameters on the weld width, weld penetration depth, resistance length, and shearing force during welding of martensitic stainless steel. They used the general full-factorial design as a DOE to find the significant factors and develop mathematical models relating the welding parameters to each of the four output responses of weld. It was found that laser power and welding speed in the range of 855–930 W and 4.5–4.65 m/min and 300 μm of fiber diameter obtained stronger and better welds.

1.1 Art section

Some previous researches on Inconel superalloy are about the effect of heat treatment on microstructure and tensile properties [14–16], and others are about the solidification, depositions, and fabrication of these alloys [17–19]. There is a noticeable lack of papers on the effect of laser parameters and their interaction on mechanical properties of Inconel superalloy which is clearly observed. From literature review, as noted in Section 1, it can be found out that DOE is a useful tool to optimize various processes as used by Pan et al. [20] and Lee et al. [21] and also welding parameters affected the quality of the weld [22]. So in the current work, central composite design of response surface methodology (RSM) was used to develop a model to predict the weld strength and microhardness deviation from that of the base metal and its correlations with microstructure of the welds in butt welded Inconel 625 strips.

2 Experimental procedure

2.1 Experimental design

Response surface method was used as a statistical analysis technique to investigate relationship between the input factors and the responses. In this method, k input factors with n levels (in terms of value) are selected. Random combination of these values forms the design matrix. The mathematical model will be developed based on the result of these experiments. This model will be used to predict the responses with different values of input parameters. In RSM, a second-order polynomial equation is used to represent the response surface "Y" as follows [23]:

$$Y = b_0 + \sum b_i x_i + \sum \beta_{ii} x_i^2 + \sum \sum b_{ij} x_i x_j + \varepsilon \qquad (1)$$

From a literature review [13, 24–28], three important factors (laser power, welding speed, and spot size as a function of focal position) in laser welding that influence the quality of the weld were selected. The process input parameters and their levels are shown in Table 1. In this study, three-level three-factor design with 20 runs was employed to develop mathematical models. Table 3 shows the random combination of the parameters and their assignment to the design matrix. Analysis of variance was performed and significant linear and interaction terms were measured. By using these mathematical models, optimal setting of welding parameters to achieve desired weld quality can be determined.

2.2 Experimental work

The superalloy material used in this study was Inconel 625 strips with 0.5-mm thickness. The chemical composition of the base metal is shown in Table 2. Autogeneous butt weld joints were made on base material coupons (Fig. 1), with weld bead running across the rolling direction, using a pulsed Nd:YAG laser welding

Table 2 Chemical composition of the base metal (in wt.%)

Ni	C	Si	S	Cr	Mo	Fe	Al	Co	Cu	Nb	Ta	TiMg
67.24	0.023	0.057	0.001	20.720	8.030	0.319	0.099	0.087	0.024	3.090	0.045	0.2270.038

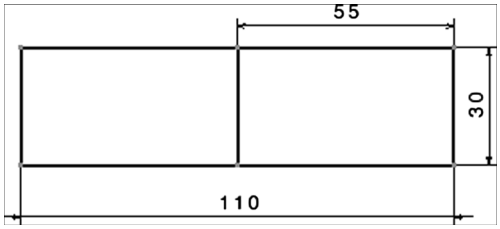

Fig. 1 Geometry and dimensions of the weld samples (mm)

machine IQL-10 with a nominal power of 400 W. Laser head was static and the table of machine moved at a controlled speed in front of nuzzle. For this purpose, a fixture as shown in Fig. 2 was used. To find out the limits of the process parameters for achieving acceptable welds, a large number of trail runs were performed. During welding operation, argon was supplied as a shielding gas at a constant flow rate of 10 l/min above the workpiece. The tensile specimens were cut from the welded strips by Charmilles Robofil 600 computer numerically controlled wire electrodischarge machine (EDM) and prepared as per the ASTM standard-E8/E8M specifications [29]. Tests were conducted in a computer-controlled universal testing machine Zwick/Roel 100 at a crosshead speed of 2 mm/min. Vickers hardness measurements were carried out for each specimen using a load of 300 g for 15 s from the center line of weld bead to the base metal using a Matsozawa MXT70 Microhardness Testing Machine. Microhardness deviation (MHD) from the base metal microhardness was determined by using Eq. 2.

$$\mathrm{MHD} = \sum_{i=1}^{4} \frac{(x_i - x_{b.m})^2}{4} \tag{2}$$

where x_i is microhardness of point I and $x_{\mathrm{b.m}}$ is base metal microhardness.

To produce specimens for microstructure study, welding specimens were sectioned transverse to the welding direction and prepared by standard metallographic procedure. The polished specimens are etched by marble's solution (10 g $CuSO_4$+50 ml HCl+50 ml H_2O) to reveal the microstructure. A Leitz Wetzlar Aristomet optical microscope was used to carry out microstructural examinations. VEGA TESCAN SEM machine was employed for more accurate investigation of microstructure of specimens.

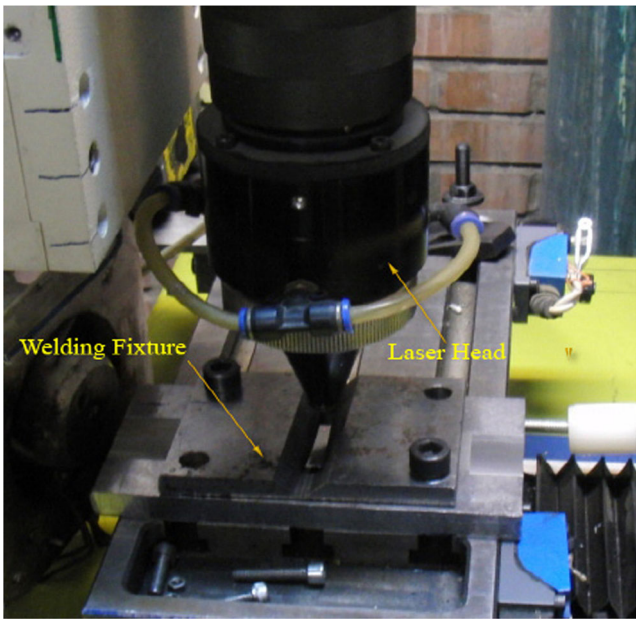

Fig. 2 Experimental setup

3 Results and discussion

The results of weld strength and microhardness tests are shown in Table 3. All the experimental results were analyzed through RSM by using Minitab 16 software package.

Table 3 Design matrix and experimental measured responses

Std ord.	Run ord.	LP	SS	WS	WST (MPa)	M.H.D (Vickers)
11	1	0	−1	0	850	17.6947
12	2	0	1	0	700	15.1060
10	3	1	0	0	1200	20.5128
14	4	0	0	1	820	16.1140
1	5	−1	−1	−1	720	20.7195
15	6	0	0	0	915	17.0520
4	7	1	1	−1	1120	23.8500
18	8	0	0	0	769	20.1535
5	9	−1	−1	1	453	8.4323
19	10	0	0	0	800	14.6702
2	11	1	−1	−1	1280	27.5562
20	12	0	0	0	900	18.1290
3	13	−1	1	−1	650	7.0840
13	14	0	0	−1	900	23.3077
17	15	0	0	0	812	19.1187
9	16	−1	0	0	650	11.6062
16	17	0	0	0	800	16.8538
8	18	1	1	1	1050	17.1395
7	19	−1	1	1	500	6.0053
6	20	1	−1	1	1180	15.0123

Table 4 ANOVA table for WST

Source	df	Sum of square	Mean square	*F* value	*p* value	
LP	1	816,245	816,245	364.36	<0.0001	Significant
SS	1	21,437	21,437	9.57	0.009	Significant
WS	1	44,489	44,489	19.86	0.001	Significant
LP^2	1	25,812	25,812	11.52	0.005	Significant
SS^2	1	11,592	11,592	5.17	0.042	Significant
LPSS	1	8911	8911	3.98	0.069	Significant
LPWS	1	7626	7626	3.40	0.090	Significant

Table 5 ANOVA table for M.H.D

Source	df	Sum of square	Mean square	*F* value	*p* value	
LP	1	252.24	252.24	81	<0.0001	Significant
SS	1	40.93	40.93	13.14	0.003	Significant
WS	1	158.52	158.52	50.90	<0.0001	Significant
LP2	1	20.57	20.57	6.60	0.023	Significant
LPSS	1	26.22	26.22	8.42	0.012	Significant
SSWS	1	36.30	36.30	11.66	0.005	Significant

Table 6 Sequential model sum of squares for WST model

R-squared 97.18 %		Adjusted *R*-squared 95.53 %			Predicted *R*-squared 92.49	
Source	df	Sum of square	Mean square	*F* value	*p* value	
Model	8	924,719	1321.03	58.97	<0.0001	Significant
Linear	3	882,171	294,057	131.26	<0.0001	Significant
Quadratic	2	26,011	13,005	5.81	0.031	Significant
2FI	3	16,537	8269	3.69	0.056	Significant
Residual	11	26,882	2240			
Lack of fit	6	8955	1279	0.36	0.894	Insignificant

Table 7 Sequential model sum of squares for M.H.D model

R-squared 92.96 %		Adjusted *R*-squared 89.71 %			Predicted *R*-squared 80.33	
Source	df	Sum of square	Mean square	*F* value	*p* value	
Model	6	534.78	89.129	28.62	<0.0001	Significant
Linear	3	451.68	150.561	48.35	<0.0001	Significant
Quadratic	1	20.57	20.57	6.60	0.023	Significant
2FI	2	62.53	31.26	10.04	0.002	Significant
Residual	13	40.48	3.114			
Lack of fit	8	21.96	2.745	0.74	0.664	Insignificant

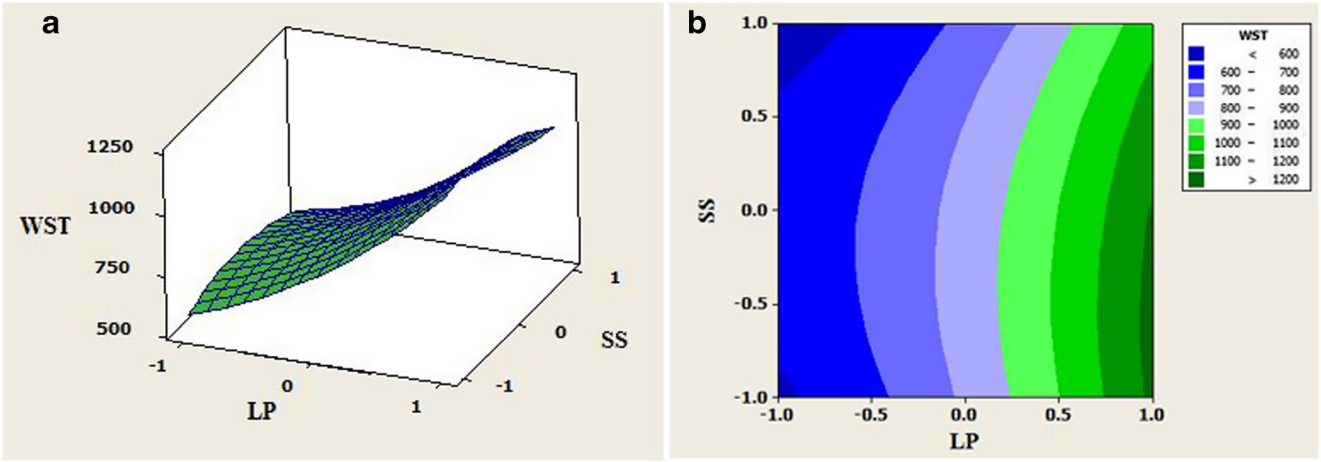

Fig. 3 Effect of LP and SS on WST **a** surface plot and **b** contour plot

3.1 Data analysis

3.1.1 Analysis of variance

The result of ANOVA for the weld strength and microhardness after elimination of insignificant factors from a model is shown in Tables 4 and 5. As can be seen, all three input parameters, quadratic (LP*LP) and (SS*SS) and two-factor interactions (2FI) of (LP*SS) and (LP*WS), are the significant model terms associated with the weld strength, and in the case of microhardness, linear factors, quadratic (LP*LP) and 2FI of (LP*SS) and (SS*WS), are the significant terms of model. Furthermore, LP is the most significant factor affecting the weld strength, whereas laser power and welding speed have a higher effect on microhardness deviation.

3.1.2 Development of mathematical models

From Tables 6 and 7, it is evident that linear, 2FI, and quadratic models are statistically significant for weld strength and microhardness. Thus, the linear, 2FI, and quadratic models were used to explain the mathematical relationship between the independent variable and dependent responses.

Using the same statistical software package, the significant coefficients were determined and final models were developed using significant coefficients to estimate WST and MHD values of the weld joint. The final mathematical models are given by

$$\begin{aligned} \mathrm{WST} = {} & 836.638 + 285.700LP - 46.300SS - 66.700\mathrm{WS} \\ & + 89.812LP^2 - 60.187\mathrm{SS}^2 - 33.375\mathrm{LP} \times \mathrm{SS} \\ & + 30.875\mathrm{LP} \times \mathrm{WS} \end{aligned} \tag{3}$$

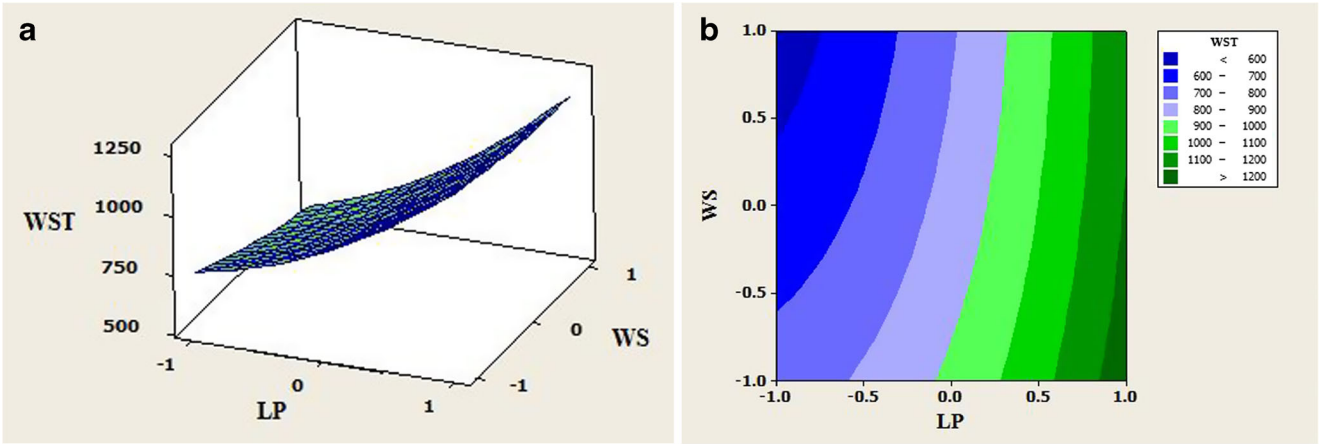

Fig. 4 Effect of LP and WS on WST **a** surface plot and **b** contour plot

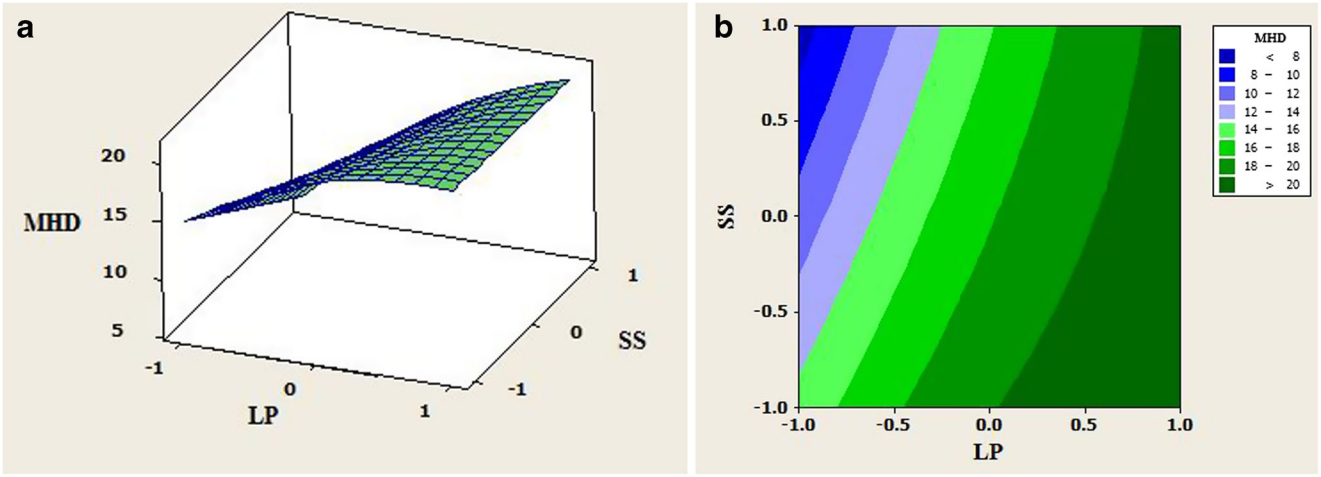

Fig. 5 Effect of LP and SS on MHD **a** surface plot and **b** contour plot

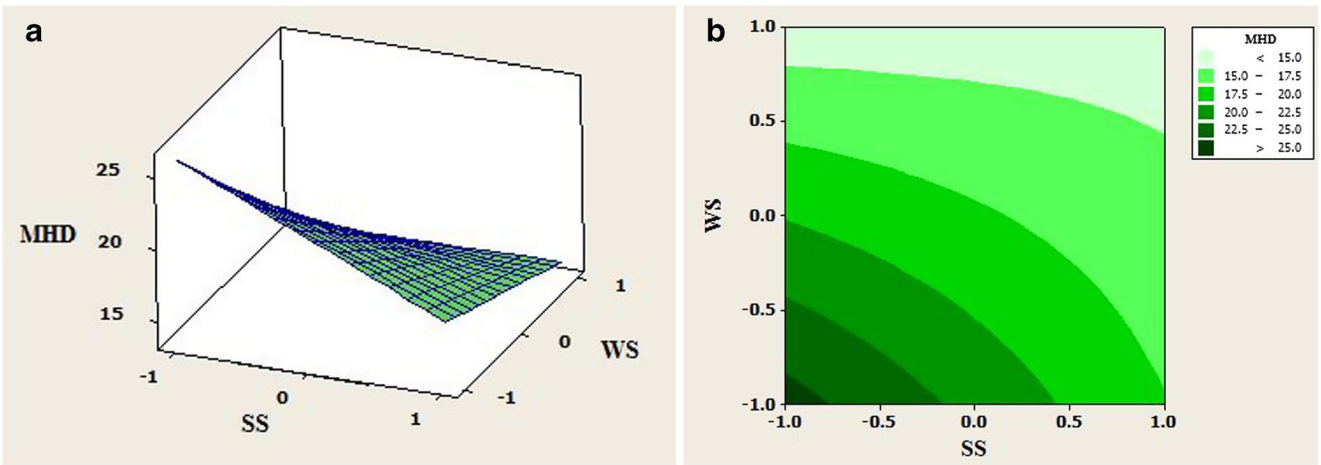

Fig. 6 Effect of SS and WS on MHD **a** surface plot and **b** contour plot

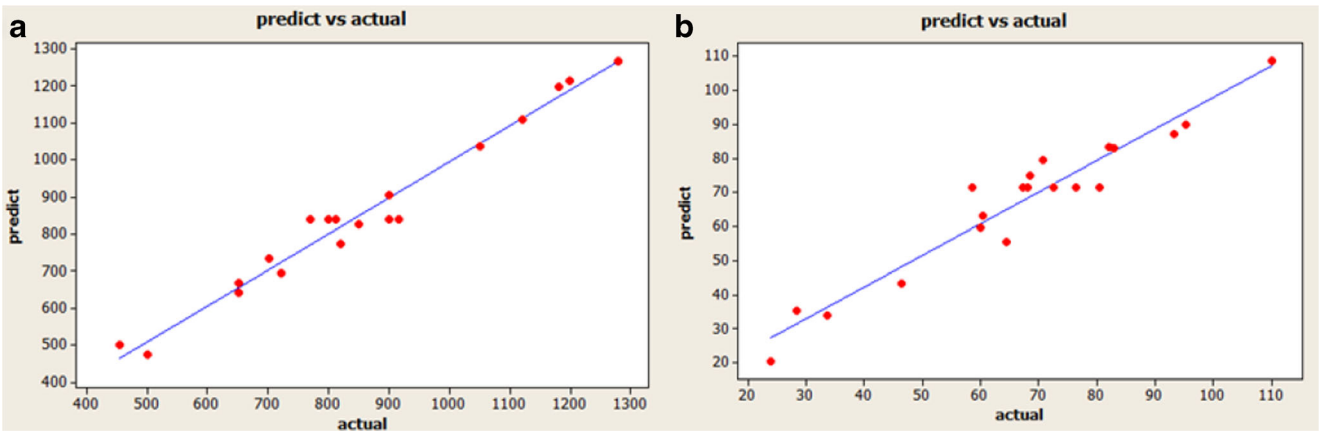

Fig. 7 Actual versus the predicted values **a** for weld strength and **b** for microhardness deviation

Table 8 Confirmation experiments

	Input parameters			Responses		
	LP (W)	SS (μm)	WS (mm/s)	Weld strength (MPa)		Microhardness deviation (Vickers)
Exp.1	260	540	3.6	Actual	1012	86.600
				Predict	1074.288	82.404
				Error	(%) −6.15	4.84
Exp. 2	260	360	1.2	Actual	1223	101.301
				Predict	1249.975	99.18
				Error	(%) −2.20	2.09

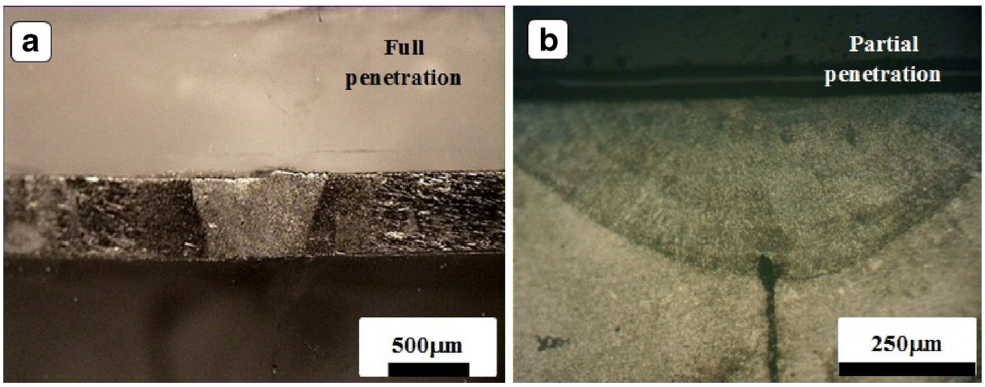

Fig. 8 Optical micrograph of sample No. **a** 8 and **b** 19

$$\mathrm{MHD} = 17.820 + 5.022\mathrm{LP} - 2.023\mathrm{SS} - 3.981\mathrm{WS} - 2.028\mathrm{LP}^2 + 1.810\mathrm{LP} \times \mathrm{SS} + 2.130\mathrm{SS} \times \mathrm{WS} \quad (4)$$

The positive sign of a coefficient indicates a synergistic effect, while a negative sign represents an antagonistic effect. The F and p values of the models connote that the selected models are highly significant. R-squared, adjusted R-squared, and predicted R-squared values of 97.18, 95.53, and 92.49 % for WST model and 92.96, 89.71, and 80.33 % for MHD model given in Tables 6 and 7 showed that the models are highly reliable. Figures 3, 4, 5, and 6 show the effect of

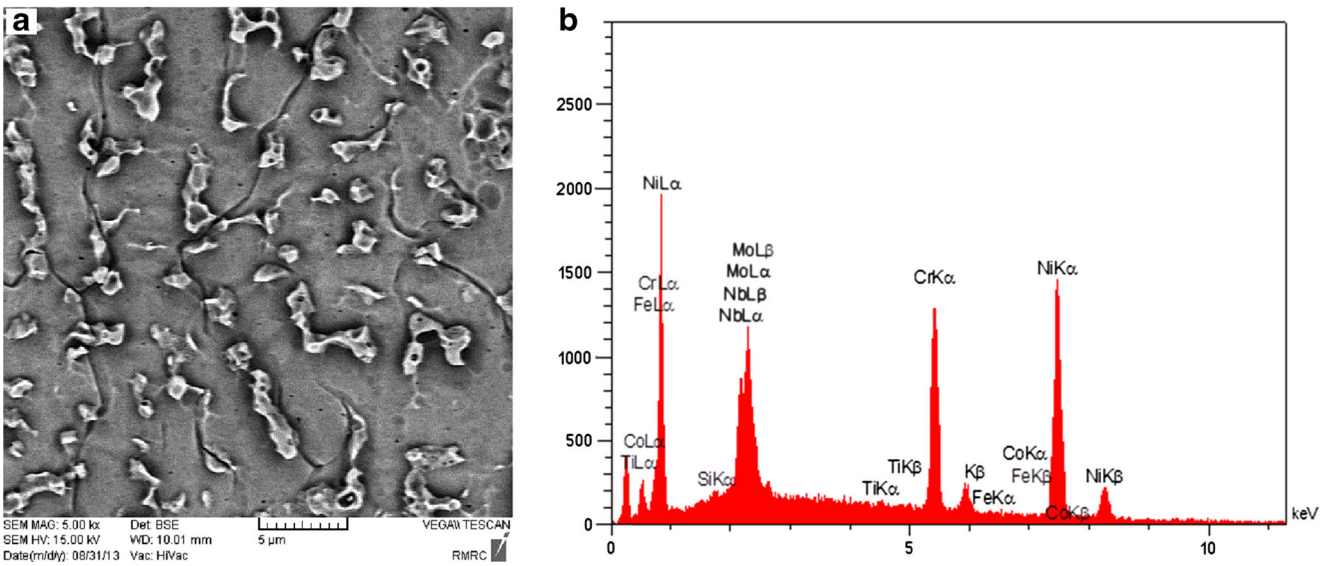

Fig. 9 **a** SEM micrograph of Laves phase particles. **b** EDS of Laves phase particles

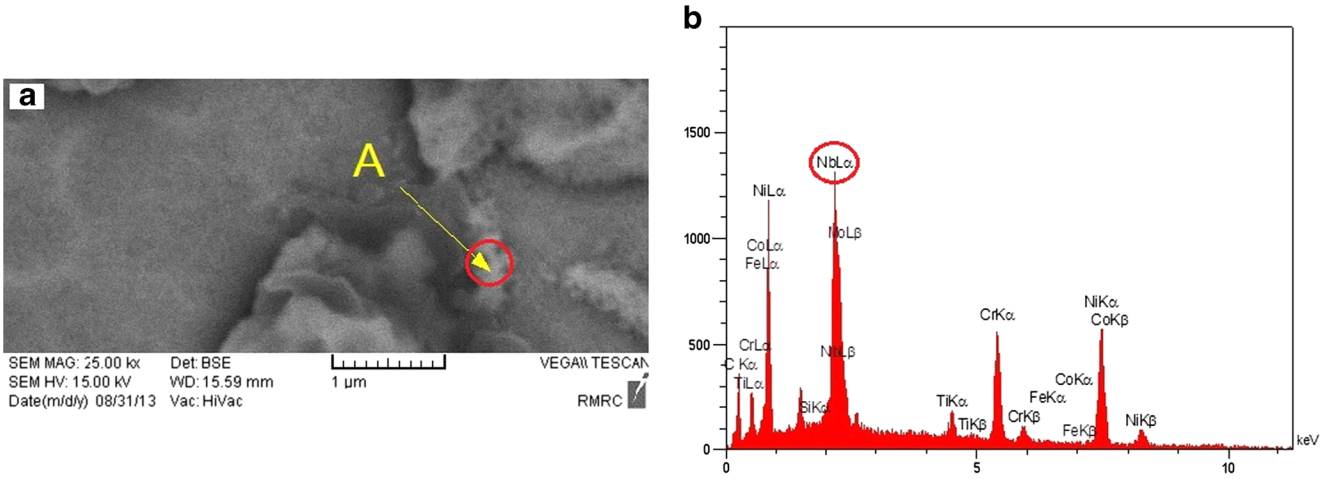

Fig. 10 **a** SEM micrograph and **b** EDS of NbC formed in sample No. 11 (Symbol "A" display the locations at which the NbC phase has been distributed)

significant model terms and their interactions on WST and MHD. From these two- and three-dimensional plots, it is concluded that WST increases with the value of LP and decreases with WS and SS, while MHD decreased with LP and the value of WS and SS. An increase in the WS results in a decrease in the weld penetration that can cause weaker weld joint as described by Han et al. [30]. An increase in the LP and decrease in the SS and WS increase the WST. MHD increases with an increase in LP, whereas SS and WS have a reverse effect. The relationship between the above parameters is expressed by the following equation [31]:

$$\mathrm{ED} = \frac{\mathrm{LP}}{\mathrm{WS} \times \mathrm{ss}} \tag{5}$$

An increase in the energy density (ED) increases the heat input to the joint, which in turn increases the penetration depth as described by M.M.A Khan [13]. Therefore, it can cause joints with higher weld strength. Therefore, Eq. (5) confirms the obtained investigation results.

3.1.3 Checking the adequacy of the developed models

Figure 7 presents plots of the actual values versus the predicted values of WST and MHD. These figures reveal that the developed models are adequate because actual and predicted values are close to each other within the specified limits. Moreover, confirmation tests were carried out to verify the adequacy of the developed models. Table 8 summarizes the experimental conditions, actual values, predicted values, and

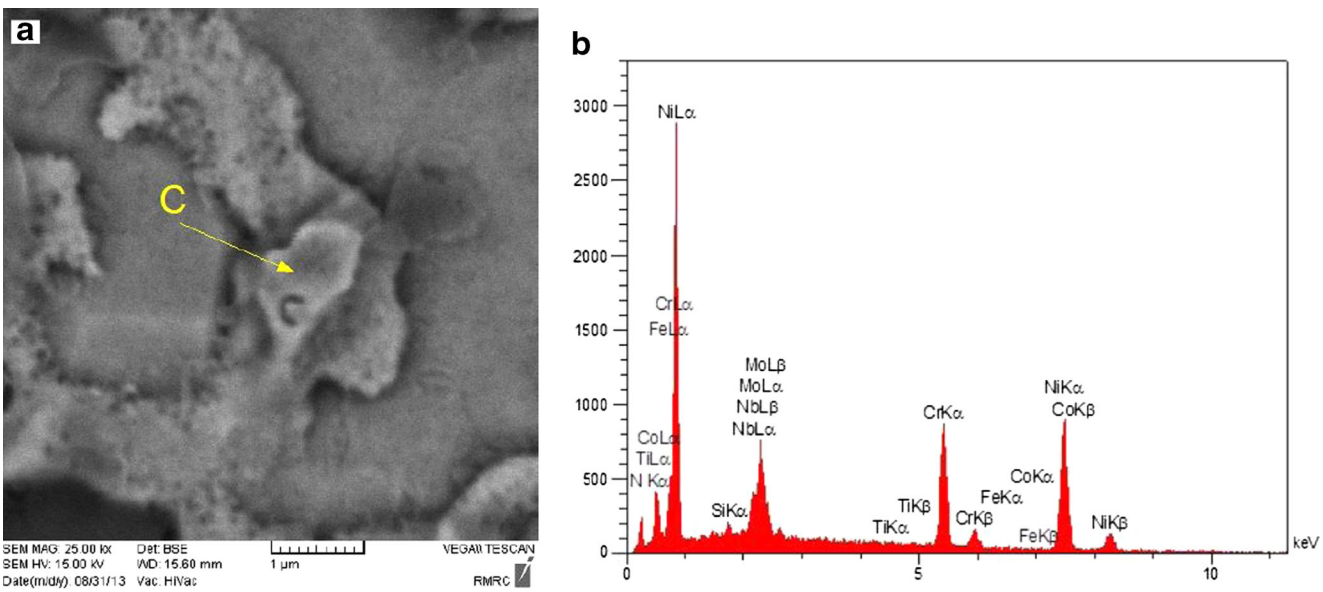

Fig. 11 **a** SEM micrograph and **b** EDS of $Ni_2(Cr, Mo)$ phase formed in sample No. 8

percentages of error. In case of MHD, because the data were divided by 4 (Eq. 2), regression coefficients are divided by 4 subsequently and the values that are obtained from the mathematical model needed to multiply by 4 to obtain correct values. The experimental results also confirm the adequacy of the developed models.

4 Microstructure

The appearance and macrostructure of the weld are illustrated in Fig. 8. According to Fig. 8, it is observed that the depth of penetration increases with an increase in the heat input. This is the main reason for increasing the WST with increasing the heat input. In other words, the depth of penetration has a greater effect than the microstructure. In addition, the microstructure of the weld is presented in Fig. 9. The microstructure shows a fully dendritic arrangement, at which a dispersive and massive precipitation in the interdendritic locations has happened (Fig. 9a). Applying a higher energy density results in more growth of dendrites that can decrease the WST properties. A higher heat input also would result in a slow cooling rate and more time available for segregation of the Si, Mo, and Nb to the interdendritic spaces and so a large volume of Laves phase and greater chance to hot cracking. Segregation and formation of the Laves phases with its EDS is shown in Fig. 9b.

Higher MHD in the weld samples with higher heat input is due to dispersion of Laves phases. Laves phase particles result in higher microhardness and so microhardness deviation from that of the base metal. As mentioned above, a higher heat input causes a slower cooling rate and the elements such as Si, Mo, and Nb can be rejected into the interdendritic regions. Figures 10 and 11 show the NbC carbide and $Ni_2(Cr, Mo)$ phase that formed in the samples No. 11 and 8, respectively, that received a higher heat input. The pick of Nb is specified on the EDS analysis, which shows the formation of high Nb containing NbC phase. NbC carbides and $Ni_2(Cr, Mo)$ phase resulted in the increase of microhardness. It is known that formation of Laves and NbC carbides can affect the weldability of superalloys and deteriorate their resistance to the solidification cracking [32].

5 Conclusions

(i) Response surface method can be used to optimize the laser welding process parameters and predict the mechanical properties of the welds, and the developed model is an admissible approach to predict the responses.

(ii) 95.53 % of data for WST model and 89.71 % data for MHD model are fitted by the developed models.

(iii) Weld strength and microhardness deviations increased with the increase in laser power. In fact, these values reach from 500 MPa and 6.0053 to 1280 MPa and 27.5562, respectively, when laser power increased from 230 to 260 W

(iv) A maximum WST of 1280 MPa was obtained for the input parameter combination of laser power of 260 W, welding speed of 1.2 mm/s, and spot size of 180 μm.

(v) Laser power of 230 W, welding speed of 6 mm/s, and spot size of 540 μm are the optimal setting of welding parameters to obtain a weld joint with a minimum MHD of 24.021.

(vi) A higher heat input resulted in a higher penetration depth and higher susceptibility to crack and high volume of Laves phases. But penetration depth had a greater effect on weld strength.

(vii) Dispersion of Laves phase particles resulted in the increase of microhardness that was observed in the samples that had experienced the highest heat input.

References

1. Cai D, Nie P, Shan J, Liu W, Gao Y, Yao M (2006) Precipitation and residual stress relaxation kinetics in shot-peened Inconel 718. J Mater Eng Perform 15(5):614–617
2. Mathew MD, Parameswaran P, Rao KBS (2008) Microstructural changes in alloy 625 during high temperature creep. Mater Charact 59(5):508–513
3. Silva CC, de Miranda HC, Motta MF, Farias JP, Afonso MCR, Ramirez AJ (2013) New insight on the solidification path of an alloy 625 weld overlay. J Mater Res Technol 32:1–10
4. Shankar V, Rao SKB, Mannan SL (2001) Microstructure and mechanical properties of Inconel 625 superalloy. J Nucl Mater 288: 222–232
5. Kuo CP, Ling CC, Chen SH, Chang CW (2005) The prediction of cutting force in milling Inconel-718. Int J Adv Manuf Technol 27: 655–660
6. Zaharinie T, Yusof F, Hamdi M, Ariga T, Moshwan R (2014) Effect of brazing temperature on the shear strength of Inconel 600 joint. Int J Adv Manuf Technol 73:1133–1140
7. Egbewande AT, Buckson RA, Ojo OA (2010) Analysis of laser beam weldability of Inconel 738 superalloy. Mater Charact 61: 569–574
8. Pandey AK, Dubey AK (2013) Modeling and optimization of kerf taper and surface roughness in laser cutting of titanium alloy sheet. J Mech Sci Technol 27(7):2115–2124
9. Huang Q, Hagstroem J, Skoog H, Kullberg G (2009) Effect of laser parameter variation on sheet metal welding. Int J Join Mater 3(1991):79–88
10. Yang YK, Chuang MT, Lin SS (2009) Optimization of dry machining parameters for high-purity graphite in end milling process via design of experiments methods. J Mater Process Technol 209: 4395–4400
11. Alrbaey K, Wimpenny D, Tosi R, Manning W, Moroz A (2014) On optimization of surface roughness of selective laser melted stainless steel parts: a statistical study. J Mater Eng Perform 23:2139–2148

12. Kim C, Choi W, Kim J, Rhee S (2008) Relationship between the weldability and the process parameters for laser-TIG hybrid welding of galvanized steel sheets. Mater Transp 49:179–186
13. Khan MMA, Romoli L, Fiaschi M, Dini G, Sarri F (2011) Experimental design approach to the process parameter optimization for laser welding of martensitic stainless steels in a constrained overlap configuration. Opt Laser Technol 43:158–172
14. Janaki Ram GD, Reddy AV, Rao KP (2005) Microstructure and tensile properties of Inconel 718 pulsed Nd:YAG laser welds. J Mater Process Technol 167:73–82
15. Cao X, Rivaux B, Jahazi M, Cuddy J, Birur A (2009) Effect of pre- and post-weld heat treatment on metallurgical and tensile properties of Inconel 718 alloy butt joints welded using 4 kW Nd:YAG laser. J Mater Sci 44:4557–4571
16. Egbewande AT, Zhang HR, Sidhu RK, Ojo OA (2009) Improvement in laser weldability of INCONEL 738 superalloy through microstructural modification. Metall Mater Trans 40A: 2694–2704
17. Amato KN, Hernandez J, Murr LE, Martinez E, Gaytan SM, Shindo PW (2012) Comparison of microstructures and properties for a Ni-base superalloy (alloy 625) fabricated by electron and laser beam. J Mater Sci Res 1:3–41
18. Xu F, Lv Y, Liu Y, Shu F, He P, Xu B (2013) Microstructural evolution and mechanical properties of Inconel 625 alloy during pulsed plasma arc deposition process melting. J Mater Sci Technol 29(5):480–488
19. Abioye TE, Folkes J, Clare AT (2013) A parametric study of Inconel 625 wire laser deposition. J Mater Process Technol 213: 2145–2151
20. Pan LK, Wang CC, Hsiao YC, Ho KC (2005) Optimization of Nd: YAG laser welding onto magnesium alloy via Taguchi analysis. Opt Laser Technol 37(1):33–42
21. Lee HK, Han HS, Son KJ, Hong SB (2006) Optimization of Nd: YAG laser welding parameters for sealing small titanium tube ends. Mater Sci Eng 415(1–2):149–155
22. Salonitis K, Stavropoulos P, Fysikopoulos A, Chryssolouris G (2013) CO2 laser butt-welding of steel sandwich sheet composites. Int J Adv Manuf Technol 69(1–4):245–256
23. Montgomery DC (2004) Design and analysis of experiments, 6th edn. John Wiley and Sons, New York
24. Qu F-S, Liu X-G, Xing F, Zhang K-F (2012) High temperature tensile properties of laser butt-welded plate of Inconel 718 superalloy with ultra-fine grains. Trans Nonferrous Metals Soc China 22: 2379–2388
25. Chen HC, Pinkerton AJ, Li L (2011) Fibre laser welding of dissimilar alloys of Ti-6Al-4V and Inconel 718 for aerospace applications. Int J Adv Manuf Technol 52:977–987
26. Acherjee B, Misra D, Bose D, Venkadeshwaran K (2009) Prediction of and seam width for laser transmission welding of thermoplastic using response surface methodology. Opt Laser Technol 41:956–967
27. Park YW, Rhee S (2008) Process modeling and parameter optimization using neural network and genetic algorithms for aluminum laser welding automation. Int J Adv Manuf Technol 37:1014–1021
28. Nakhaei MR, Mostafa Arab NB, Naderi G (2013) Application of response surface methodology for prediction in laser welding of polypropylene/clay nanocomposite. Iran Polym J 22:351–360
29. Standard test methods for tension testing of metallic materials, E 8M–04, annual book of ASTM Standards, ASTM, 1–24
30. Han WJ, Byeon JG, Park KS (2001) Welding characteristics of the Inconel plate using a pulsed Nd: YAG laser beam. J Mater Process Technol 113:234–237
31. Childs THC, Berzins M, Ryder GR, Tontowi AE (1999) Selective laser sintering of an amorphous polymer: simulations and experiments. Proc Inst Mech Eng B J Eng Manuf 213:333–349
32. Naffakh-Moosavy H, Aboutalebi M-R, Seyedein SH (2012) An analytical algorithm to predict weldability of precipitation-strengthened nickel-base superalloys. J Mater Process Technol 212:2210–2218